PCCP

Physical Chemistry Chemical Physics

www.rsc.org/pccp

Volume 15 | Number 34 | 14 September 2013 | Pages 14133–14512

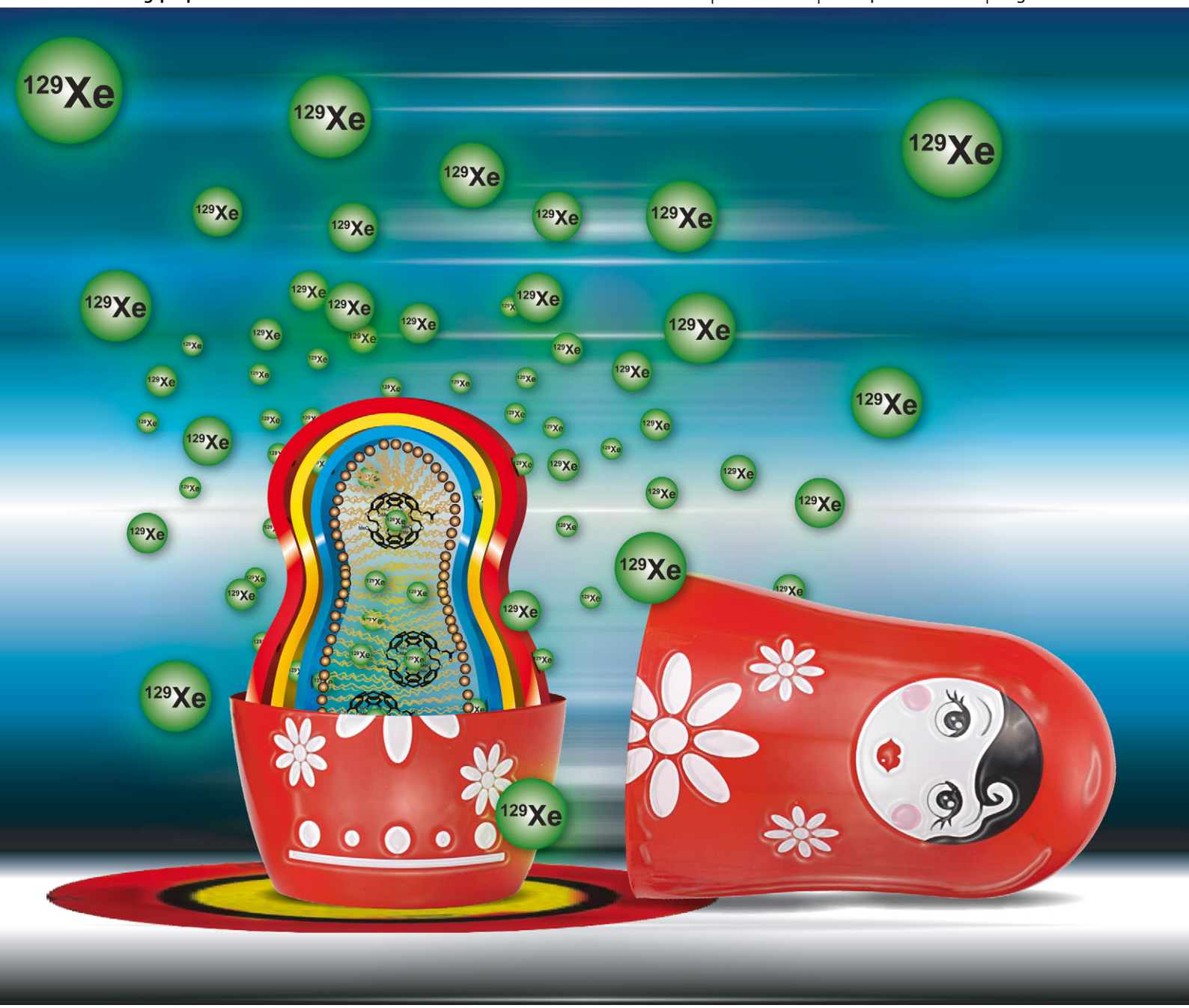

ISSN 1463-9076

COMMUNICATION

Schnurr *et al.*

Functionalized ^{129}Xe as a potential biosensor for membrane fluidity

PCCP

RSC Publishing

COMMUNICATION

View Article Online
View Journal | View Issue

Functionalized ^{129}Xe as a potential biosensor for membrane fluidity†

Cite this: *Phys. Chem. Chem. Phys.*, 2013, **15**, 14178

Received 21st March 2013,
Accepted 6th June 2013

DOI: 10.1039/c3cp51227d

www.rsc.org/pccp

Matthias Schnurr,* Christopher Witte and Leif Schröder*

Using spin hyperpolarized xenon (^{129}Xe) we investigate the impact of the local molecular environment on reversible host–guest interactions. We label Xe guest atoms that are temporarily bound to cryptophane-A hosts using the Hyper-CEST technique. By varying the length of the saturation pulse and utilizing an inverse Laplace transform we can determine depolarization times for the noble gas in different local environments, in this case biomembranes possessing different fluidity. We extend this technique to magnetic resonance imaging, mapping the spatial distribution of the different biomembranes. Such decays measured in biomembranes of 200 μM 1-palmitoyl-2-oleoyl-*sn*-*glycero*-3-phosphocholine (POPC) and 1,2-dipalmitoyl-*sn*-*glycero*-3-phosphocholine (DPPC) were characterized by mono-exponential decays with time constants of $\tau_{POPC} = 3.00^{+0.77}_{-0.61}$ s and $\tau_{DPPC} = 22.15^{+5.19}_{-4.16}$ s. Analyzing both environments simultaneously yielded a bi-exponential decay. This approach may give further insights into saturation transfer dynamics of reversibly bound Xe with applications extending into biomedical diagnostics.

NMR of hyperpolarized ^{129}Xe combines both the high sensitivity of up to a 10^5-fold increased detectable magnetization over the thermally polarized gas with the high specificity from a large chemical shift range.[1] Xe can be embedded into different environments and can carry various types of information in its NMR signal. Recently Stupic *et al.* used Xe as an additive in a flammable gas to perform velocimetry for transport processes in combustors.[2] This represents quantification of atom displacement in a directed flow on a macro- or mesoscopic scale. Random motion such as diffusion of atoms on a microscopic scale, however, can also be studied using NMR, either in a very general way by analyzing relaxation times (both T_1 and T_2 depend on the correlation time of molecular tumbling) or by applying magnetic field gradients for diffusion weighting. However, such experiments are not always possible since they require sufficient signal intensity and unambiguous resonance assignment when working with emulsions where Xe can reversibly access more than one environment. Investigating the behavior of Xe inside phospholipid membranes in aqueous solutions is such a case. The hydrophobic gas shows high solubility in lipid environments.[3] However, any conventional relaxivity or diffusion study would be hampered by fast chemical exchange between membrane-embedded Xe and Xe in an aqueous environment. We therefore studied an approach in which the intra-membrane mobility of the atoms is probed indirectly.

Xe exhibits great potential for applications in biosensors[4] that bind to membrane-bound receptors,[5,6] potentially followed by cellular uptake.[7] To this end, induced Xe spin depolarization inside cryptophane-A-monoacid cages (CrA_{ma}) can be used as a mechanism that is sensitive to Xe mobility. The cages can reversibly bind the noble gas atoms. This host–guest system enables multiple features: (i) it separates the spin pool into two spectrally distinct populations[8,9] enabling selective depolarization through RF irradiation and (ii) it establishes a steady state of reversible binding events where the Xe access to the cage regulates the replenishment of hyperpolarized nuclei for membrane-embedded host sites. Moreover, the driven depolarization of exchangeable, hyperpolarized nuclei, also known as Hyper-CEST,[10] provides a significant signal enhancement that allows studying concentrations in the fM–nM range,[11,12] even for MR imaging applications.[13] The induced depolarization is observed as it accumulates in the pool of non-caged Xe and causes the corresponding signal to decrease. The by far larger fraction of dissolved Xe in dilute phospholipid solutions is found in the aqueous environment. Xe that participates in the labeling procedure has to penetrate into the membrane, travel to host sites and escape back into the water pool to transport the information from induced depolarization. Hence, differences in membrane fluidity are expected (amongst other effects) to influence the efficiency of this process reflected in the intensity and build-up of the CEST response.

Zaiss *et al.* showed that on-resonant saturation pulses with increasing saturation times t_{sat} yield a mono-exponential depolarization process[14]

$$f(\tau, t_{sat}) = e^{-t_{sat}/\tau(k, T_2, \phi)}. \quad (1)$$

Leibniz-Intitut für Molekulare Pharmakologie (FMP), ERC Project BiosensorImaging, Robert-Rössle-Str. 10, 13125 Berlin, Germany. E-mail: schnurr@fmp-berlin.de, lschroeder@fmp-berlin.de; Tel: +49 (0)3094793121

† Electronic supplementary information (ESI) available: Experimental details, RAW data images, the ILT procedure and supporting figures. See DOI: 10.1039/c3cp51227d

Where τ is the depolarization time, which depends on relevant system parameters such as the exchange rate k of Xe from CrA_{ma} to the surrounding medium, the relaxation time T_2 of Xe@CrA_{ma} and the local concentration ratio ϕ = [Xe@CrA_{ma}]/[Xe@solution]. This mono-exponential process has also been observed experimentally.[15]

In this work we take advantage of different τ's of functionalized Xe, arising from different Xe mobility in different molecular environments. More precisely, we prepared different small unilamellar vesicles of 1-palmitoyl-2-oleoyl-*sn-glycero*-3-phosphocholine (POPC) and 1,2-dipalmitoyl-*sn-glycero*-3-phosphocholine (DPPC), where the latter possesses a lower membrane fluidity below 40 °C.[16,17] The different τ's in the two biomembranes generate a new tunable MRI contrast even if the encapsulated Xe experiences similar chemical shifts. The τ's of the (multi-)exponential decays are obtained *via* an algorithm using the Laplace transform (LT) and the inverse LT (ILT). Hence the requirement for the detection of caged Xe in different molecular environments with similar chemical shifts is a difference in k, T_2 or ϕ, which is large enough to yield medium differences in τ. Too pronounced differences in τ might make slow depolarization invisible when a process with much shorter τ happens at the same time in the same micro-environment.

Fig. 1 illustrates how different Hyper-CEST signals can have the same chemical shift, which are therefore not resolved according to their resonance frequency. CEST-spectra of solutions containing 5 μM CrA_{ma} with 200 μM POPC or 200 μM DPPC at 9.4 T and 303 K are displayed. Two CEST responses are visible throughout all spectra. The one at *ca.* 64 ppm corresponds to Xe@CrA_{ma} in the aqueous solution (the gaseous Xe signal is set to 0 ppm). The broader one at *ca.* 74 ppm (Xe@CrA_{ma}@lipid) originates from *ca.* 10^{12} liposomes, each of which contains *ca.* 2000 CrA_{ma} molecules (see ESI†). This signal features a similar chemical shift for both phospholipids, POPC (red triangles (up)) and DPPC (green triangles (down)). However, the CEST response is much less intense for DPPC than for POPC. Also only a single response was detected at 74.0 ppm when we analyzed a CEST-spectrum of both solutions simultaneously in neighboring compartments (blue diamonds). The response obtained in the last experiment should be made up of a superposition of the two responses of POPC in the inner and of DPPC in the outer compartment. Thus, all three responses are similar in chemical shift but different in depletion and width. Hence, the information about differences in depolarization build-up in different compartments is lost when acquiring a global signal from the entire object.

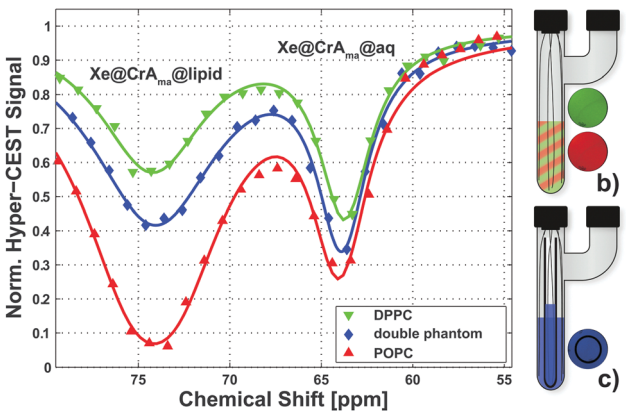

Fig. 1 CEST-spectra of 5 μM CrA_{ma} in 200 μM DPPC (green triangles (down)), 200 μM POPC (red triangles (up)) (each measured in a modified 10 mm NMR tube (b)) and the double phantom containing both solutions (blue diamonds, a 5 mm NMR tube in a 10 mm NMR tube (c)) at 9.4 T and 303 K. The response at *ca.* 64 ppm corresponds to Xe in CrA_{ma} in the aqueous solution, the response at *ca.* 74 ppm corresponds to Xe in CrA_{ma} in the lipid environment. The gaseous Xe signal is set to 0 ppm. Data points were obtained by applying a 5 s saturation pulse of B_1 = 10 μT at a desired frequency and detecting the Xe@solution signal (at 193 ppm). Sweeping the saturation pulse over the shown chemical shift range yields a CEST spectrum. The integral of the signal after off-resonant saturation (−74 ppm) is normalized to 1.

Therefore we studied the dynamics of functionalized Xe in two neighboring molecular environments by acquiring MR images of a phantom (Fig. 2a) using the Hyper-CEST EPI method[13] and applying saturation pulses at 74 ppm with variable t_{sat} (10^{-3}–20 s). As shown in Fig. 2a the signal of the outer compartment of the phantom (containing DPPC) decreased more slowly compared to the signal of the inner compartment (containing POPC). Thus, the dynamical difference in signal depletion of the two compartments is already visible when acquiring a stack of Hyper-CEST images with different saturation times. Furthermore it is possible to tune the contrast by applying saturation pulses of different lengths: for $t_{sat} < 10^{-1}$ s all phospholipid environments in which functionalized Xe is present are visible, whereas for $t_{sat} \sim 6$ s the signal related to DPPC is greater than the one related to POPC.

The measured overall Hyper-CEST signal for on-resonant (Xe@CrA_{ma}@lipid) saturation in each image in Fig. 2a should contain all contributing depolarization processes leading to a superposition weighted by their probability $F(s)\mathrm{d}s$, so that

$$f(t_{sat}) = \int_0^\infty F(s)\mathrm{e}^{-st_{sat}}\mathrm{d}s, \qquad (2)$$

where $s = 1/\tau$, $F(s) \geq 0$ and $\int_0^\infty F(s)\mathrm{d}s = 1$. Eqn (2) is the LT of $F(s)$, $\mathscr{L}\{F(s)\}$. Thus, finding its inverse $\mathscr{L}^{-1}\{f(t_{sat})\}$ yields the corresponding τ distribution. ILT is a common tool for analyzing exponential decays.[19–23] We can discretize eqn (2) and include noise ($\varepsilon_{\nu,t_{sat}}$):

$$f(t_{sat}) = \frac{\sum_{\nu=1}^{n} F(s_\nu)\mathrm{e}^{-s_\nu t_{sat}} + \varepsilon_{\nu,t_{sat}}}{\sum_{\nu=1}^{n} F(s_\nu)} \qquad (3)$$

where n is the number of molecular environments, $F(s_\nu)$ is the probability density of the signal of environment ν and τ_ν is its depolarization time. We obtain $\mathscr{L}^{-1}\{f(t_{sat})\}$ numerically (MATLAB®, modified routine *rilt.m*[24]) using a regularized non-negative least square method in 1D, developed by Provencher.[25] As the ILT analysis is ill conditioned,[26] one requires an extra condition to ensure a unique solution. Therefore Tikhonov regularization[27] is used for which $F(s)$ has to be as smooth as possible in s. In summary, the ILT analysis can determine the contributing τ's and the quantity n without any prior knowledge.

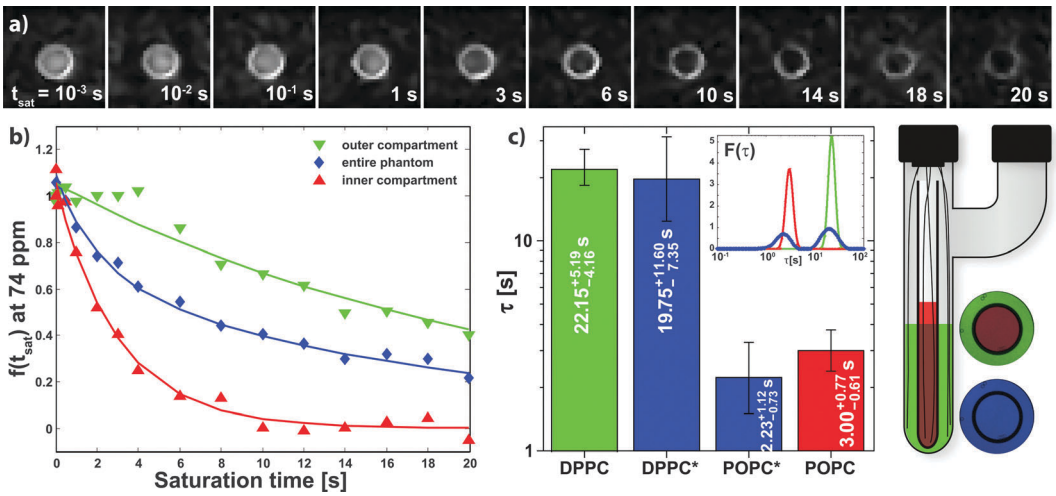

Fig. 2 Axial Hyper-CEST imaging (4 averages) of the entire phantom (a). On-resonant saturation at 74.0 ppm with B_1 = 10 μT and variable t_{sat} at 9.4 T was used. Images were smoothed using an adaptive weight filter with a local quadratic model.[18] (b) The decreasing Hyper-CEST signal $f(t_{sat})$ of the entire phantom (blue diamonds), only the outer compartment (green triangles (down)) and only the inner compartment (red triangles (up)). The solid lines are the fit results obtained from the ILT analysis. The outer compartment's noisy data might be the result of the remaining gas bubbles between the two glass walls during data acquisition. The depolarization times at the maxima of the probability density functions $F(\tau)$ (see inset) are shown in (c). When analyzing the entire phantom simultaneously $F(\tau)$ has two maxima (DPPC* and POPC*). When analyzing only the outer compartment (DPPC) or only the inner compartment (POPC) $F(\tau)$ has only one maximum.

Fig. 2b shows the measured signal decays of the entire phantom and its two individual compartments. The fits are the LTs of the τ distributions shown in the inset in Fig. 2c. Fig. 2c summarizes the depolarization times: with increasing t_{sat} the signal of the inner compartment disappeared faster ($\tau_{POPC} = 3.00^{+0.77}_{-0.61}$ s) than the signal of the outer compartment ($\tau_{DPPC} = 22.15^{+5.19}_{-4.16}$ s). When we analyzed the entire phantom containing both different environments using the ILT algorithm two τ's were found, $\tau_{POPC^*} = 2.23^{+1.12}_{-0.73}$ s and $\tau_{DPPC^*} = 19.75^{+11.60}_{-7.35}$ s. We assign the faster one to the inner compartment and the slower one to the outer compartment because both are found to be the same within errors when the compartments are analyzed alone. We ascribe the different depolarization times to differences in membrane fluidity of POPC and DPPC, as all other experimental parameters were the same (assuming similar solubility of Xe in DPPC and POPC[28]), as follows: the 7-times faster depolarization time in POPC than in DPPC is most likely caused by a 7-times higher turnover of Xe atoms partitioning into the membrane and passing through CrA_{ma} molecules in POPC than in DPPC during the length of the saturation pulse. The reasons for this can be (i) a faster overall exchange rate k' of Xe in POPC than in DPPC, which combines the exchange from CrA_{ma} to the lipid environment and the escape back into the aqueous solution, (ii) a higher concentration ratio ϕ in POPC than in DPPC or (iii) the spin–spin associated T_2 relaxation time of Xe@CrA_{ma}@lipid which might be affected by the membrane fluidity and could therefore also influence the depolarization process. According to eqn (22) in ref. 14 (Zaiss *et al.*) a longer T_2 of the Xe@CrA_{ma}@lipid should increase τ. So far it is not known whether T_2 is in the order of k^{-1} or not. We assume that it is unlikely that slightly different chemical compositions of phospholipids can induce such a large difference in τ. In all experiments the T_1 relaxation time of Xe was similar (see ESI†) and should have a minor contribution to the depolarization process. Hence, a pure T_1 analysis would not be able to reveal differences in POPC and DPPC. All the other parameters are combined in τ. Thus, it is not possible to know exactly what causes the variable depolarization times. However, membrane fluidity is the major difference between POPC and DPPC liposomes and therefore it is most likely that it is the main driver of the different τ's. The effect of membrane composition has also recently been mentioned in the context of DIACEST agents.[29] We suppose that different molecular environments which are spatially separated, as it should be the case for example for a tumor surrounded by healthy tissue, should result in more than one τ yielding a multi-exponential decay.

In addition to the analysis of the whole compartments we performed a pixel-wise ILT which yielded a certain τ for every 625 × 625 (μm)^2 pixel. The fitting took *ca.* 12 s per pixel. Fig. 3 shows the spatial distribution of the τ's in the phantom. The spatial distribution is in very good agreement with the data gained from the ILT analysis of the whole compartments (Fig. 2). The low τ's (represented in yellow) of a few pixels at the outer edge of the outer compartment probably result from partial volume effects. If the number n of maxima in $F(s)$ for a certain pixel was found to be >1 the dominant τ was assigned as that very pixel value (mainly at the edge of a compartment and in some noisy data sets; see ESI† for data for every pixel). The image illustrates the applicability of generating MR-contrast based on different τ's in different molecular environments. The need for high resolution is obvious. Otherwise one might end up with more than one possible τ for a single pixel (think of a pixel as large as the whole phantom).

In conclusion, different depolarization times in different molecular environments, such as biomembranes, of hyperpolarized Xe encapsulated in CrA_{ma} can generate a new type of MRI contrast. The contrast can be obtained by applying saturation pulses of

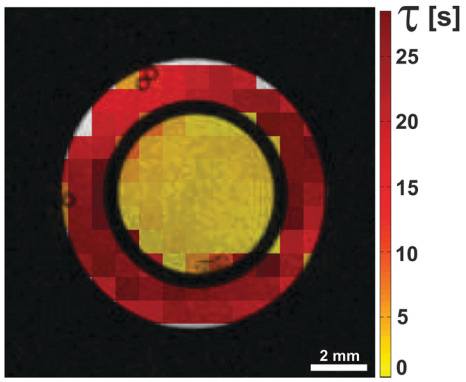

Fig. 3 Depolarization-time map of the phantom. A ^{1}H image is superimposed. For each pixel (625 × 625 (μm)^2 in plane resolution) the depolarization time is gained from the ILT analysis. See ESI† for the ILT result of every pixel.

different lengths and analyzing the decaying data using ILTs. The detection of different molecular environments does not require prior knowledge regarding the number, n, of contributing spatially separated depolarization processes as a boundary condition, as is the case when using other fitting routines. This advantage will be more evident when analyzing more challenging samples. In particular the presented method adds a new dimension to Hyper-CEST through the ability to distinguish overlapping CEST responses. When membrane fluidity was higher, the depolarization time was shorter and the Hyper-CEST signal was completely saturated at shorter saturation pulses. Still the remaining limitation of the Hyper-CEST method is the fact that it is until now not possible to clearly dissect the concentration ratio ϕ, the exchange rate k or the relaxation time T_2 which will be a focus of future research.

Acknowledgements

This work was supported by the European Research Council under the European Community's Seventh Framework Program (FP7/2007-2013)/ERC grant agreement no. 242710 and the Human Frontier Science Program. We gratefully thank Jörg Döpfert and Martin Kunth for providing the EPI sequence.

References

1 C. Witte and L. Schröder, *NMR Biomed.*, 2012, DOI: 10.1002/nbm.2873.
2 K. F. Stupic, J. S. Six, M. D. Olsen, G. E. Pavlovskaya and T. Meersmann, *Phys. Chem. Chem. Phys.*, 2013, **15**, 94–97.
3 R. D. Booker and A. K. Sum, *Biochim. Biophys. Acta, Biomembr.*, 2013, **1828**, 1347–1356.
4 M. M. Spence, S. M. Rubin, I. E. Dimitrov, E. J. Ruiz, D. E. Wemmer, A. Pines, S. Q. Yao, F. Tian and P. G. Schultz, *Proc. Natl. Acad. Sci. U. S. A.*, 2001, **98**, 10654–10657.
5 G. K. Seward, Y. Bai, N. S. Khan and I. J. Dmochowski, *Chem. Sci.*, 2011, **2**, 1103–1110.
6 K. K. Palaniappan, R. M. Ramirez, V. S. Bajaj, D. E. Wemmer, A. Pines and M. B. Francis, *Angew. Chem., Int. Ed.*, 2013, **52**, 4849–4853.
7 C. Boutin, A. Stopin, F. Lenda, T. Brotin, J.-P. Dutasta, N. Jamin, A. Sanson, Y. Boulard, F. Leteurtre, G. Huber, A. Bogaert-Buchmann, N. Tassali, H. Desvaux, M. Carrière and P. Berthault, *Bioorg. Med. Chem.*, 2011, **19**, 4135–4143.
8 T. Meldrum, L. Schröder, P. Denger, D. E. Wemmer and A. Pines, *J. Magn. Reson.*, 2010, **205**, 242–246.
9 J. Sloniec, M. Schnurr, C. Witte, U. Resch-Genger, L. Schröder and A. Hennig, *Chem.–Eur. J.*, 2013, **19**, 3110–3118.
10 L. Schröder, T. J. Lowery, C. Hilty, D. E. Wemmer and A. Pines, *Science*, 2006, **314**, 446–449.
11 Y. Bai, P. A. Hill and I. J. Dmochowski, *Anal. Chem.*, 2012, **84**, 9935–9941.
12 L. Schröder, T. Meldrum, M. Smith, T. J. Lowery, D. E. Wemmer and A. Pines, *Phys. Rev. Lett.*, 2008, **100**, 257603.
13 M. Kunth, J. Döpfert, C. Witte, F. Rossella and L. Schröder, *Angew. Chem., Int. Ed.*, 2012, **51**, 8217–8220.
14 M. Zaiss, M. Schnurr and P. Bachert, *J. Chem. Phys.*, 2012, **136**, 144106.
15 L. Schröder, L. Chavez, T. Meldrum, M. Smith, T. J. Lowery, D. E. Wemmer and A. Pines, *Angew. Chem., Int. Ed.*, 2008, **47**, 4316–4320.
16 C. D. Stubbs, T. Kouyama, K. Kinosita and A. Ikegami, *Biochemistry*, 1981, **20**, 4257–4262.
17 G. Cevc, *Biochemistry*, 1991, **30**, 7186–7193.
18 J. Polzehl and K. Tabelow, *J. Statist. Software*, 2007, **19**, 1–17.
19 S. Peresada, A. Tonielli, R. Morici and C. S. Johnson, *Prog. Nucl. Magn. Reson. Spectrosc.*, 1999, **34**, 203–256.
20 H. Koskela, O. Heikkinen, I. Kilpeläinen and S. Heikkinen, *J. Biomol. NMR*, 2007, **37**, 313–320.
21 H. Koskela, I. Kilpeläinen and S. Heikkinen, *Magn. Reson. Chem.*, 2004, **42**, 61–65.
22 Z. Bajzer, A. C. Myers, S. S. Sedarous and F. G. Prendergast, *Biophys. J.*, 1989, **56**, 79–93.
23 J. Jakeš and P. Štěpánek, *Czech. J. Phys.*, 1990, **40**, 972–983.
24 I.-G. Marino, *rilt.m*, http://www.mathworks.com/matlabcentral/fileexchange/6523-rilt/content/rilt.m, 2007, [online; accessed 18-March-2013].
25 S. W. Provencher, *Comput. Phys. Commun.*, 1982, **27**, 229–242.
26 P. C. Hansen, *Rank-Deficient and Discrete Ill-Posed Problems: Numerical Aspects of Linear Inversion*, SIAM, 1997.
27 A. N. Tikhonov and V. I. Arsenin, *Solutions of ill-posed problems*, Winston, 1977.
28 R. A. Smith, E. G. Porter and K. W. Miller, *Biochim. Biophys. Acta, Biomembr.*, 1981, **645**, 327–338.
29 K. W. Y. Chan, G. Liu, X. Song, H. Kim, T. Yu, D. R. Arifin, A. A. Gilad, J. Hanes, P. Walczak, P. C. M. van Zijl, J. W. M. Bulte and M. T. McMahon, *Nat. Mater.*, 2013, **12**, 268–275.